Elemental Distribution and Melting Characteristics of FeNi nanoparticles on W(110) surfaces

Mahboobeh Ravankhah, Philipp Watermeyer, Gerhard Dehm, Mathias Getzlaff

Suggested Citation:
Ravankhah, M., Watermeyer, P., Dehm, G., & Getzlaff, M. (2024). Elemental Distribution and Melting Characteristics of FeNi nanoparticles on W(110) surfaces. Surface Science, 751, Article 122606.
https://doi.org/10.1016/j.susc.2024.122606

Surface Science 751 (2025) 122606

Contents lists available at ScienceDirect

Surface Science

journal homepage: www.elsevier.com/locate/susc

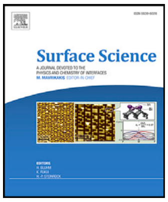

Elemental Distribution and Melting Characteristics of FeNi nanoparticles on W(110) surfaces

Mahboobeh Ravankhah [a], Philipp Watermeyer [b], Gerhard Dehm [b], Mathias Getzlaff [a,*]

[a] Institut für Angewandte Physik, Heinrich-Heine-Universität, Düsseldorf, Germany
[b] Max–Planck-Institut für Eisenforschung GmbH, Düsseldorf, Germany

ARTICLE INFO

Keywords:
FeNi nanoparticles
W(110) surface
Elemental distribution
Nanocluster
Source size distribution
Melting behavior

ABSTRACT

In this report we describe new findings on the structure, composition and thermal stability of Fe_xNi_{1-x} nanoparticles, synthesized via a magnetron sputtering source and deposited on a clean W(110) surface. The elemental distribution of the nanoparticles was determined by energy dispersive X-ray (EDX) and electron energy loss spectroscopy (EELS). The melting behavior of the nanoparticles was studied under UHV by scanning tunneling microscopy (STM) upon heating. Notably, it has been observed that the nanoparticle's core is characterized by an enrichment of Ni atoms, while the shell shows a higher amount of Fe atoms. Specifically, in the case of $Fe_{0.75}Ni_{0.25}$ and $Fe_{0.25}Ni_{0.75}$, where a Ni core is surrounded by a Fe shell, all nanoparticles completely liquefy after heating at 540 K. In contrast, the $Fe_{0.50}Ni_{0.50}$ nanoparticles, which exhibit a homogeneous distribution of both elements, only begin to melt around 540 K.

1. Introduction

The synthesis and characterization of Fe_xNi_{1-x} have received much attention in the scientific and technological fields. FeNi nanoparticles exhibit special properties, such as large magnetic moment (with crystallography L10 structure), soft magnetization and catalytic properties, which strongly depended on the geometry and configuration of atoms [1–3]. The structure of bimetallic nanoparticles can be classified into three type of systems. They can form a core–shell structure, bimetallic dimers or an alloy. FeNi nanoparticles have been prepared by several methods [4–7]. For example, crystalline FeNi nanoparticles were synthesized by reducing $NiCl_2$ and $FeCl_2$ vapor with hydrogen, in which the size distribution of nanoparticles was controlled by the gas flow rate and reaction temperature [4]. Yan Liu et al. [5] and Shao et al. [6] reported Fe–Ni alloy nanoparticles using hydrothermal method with different feeding ratio of metal, showing the morphology, thermal stability and magnetic properties of nanoparticles depend on the composition. Chemical configuration with a Ni core and Fe-Ni outer shell have been synthesized by Margeat et al. [7] and the reverse arrangement has been experimentally established in nickel-rich FeNi clusters [8]. Thus, it is not easy to say which elements tend to take surface sites or to be in the core.

In these reports the magnetic properties of nanoparticles are shown to depend on the atomic structure, chemical composition and size distribution, but there is limited information about the elemental distribution of Fe-Ni and the ability to control the composition and the structural phase.

Due to the attractive properties of bimetallic nanoparticles, this study is directed towards the synthesis of Fe-Ni nanoparticles and investigate the properties of the structure, using high resolution transmission electron microscopy. Additionally from a technological point of view, the possible use of such nanoparticles for applications include process steps of elevated temperatures. This naturally motivates to investigate the dependence of thermal stability of Fe-Ni bimetallic nanoparticles on Fe or Ni percentage by application of STM.

The relevant result could be helpful for the design and preparation of stable and controllable bimetallic nanoparticles for technological applications. A former study [9] already proved that the melting behavior of FeNi nanoparticles is significantly different to those from pure Fe and pure Co [10] as well as from an FeCo alloy [10,11].

2. Experimental methods

Nanoparticle's deposition was performed using a nanocluster source manufactured by Oxford Applied Research [12]. The particles can be selected with respect to their mass/charge ratio. For the measurement of the particle's size distribution, the quadrupole mass filter QMF200 was used. The mass selection is controlled by a frequency and the

---

* Corresponding author.
E-mail address: getzlaff@hhu.de (M. Getzlaff).

https://doi.org/10.1016/j.susc.2024.122606
Received 20 August 2024; Accepted 9 September 2024

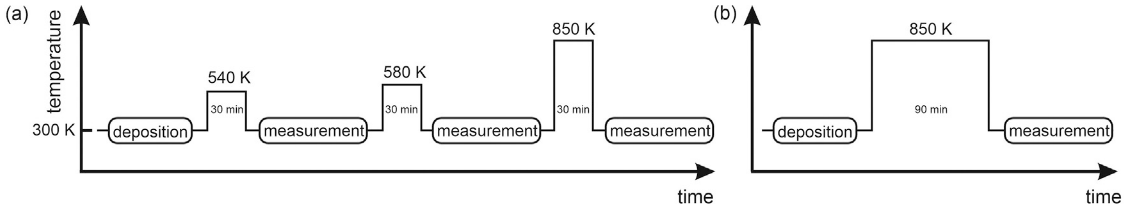

Fig. 1. A visual representation of the step-by-step heating and measuring protocol, highlighting the temperature and time intervals at each stage of the experiment.

amplitude of an ac voltage. The selected nanoparticles were deposited directly on the clean W(110) surface for STM analysis and on graphene oxide coated Cu grids for TEM analysis.

The substrate used in this work is a tungsten single crystal with a (110) surface. Before the W can be used as a substrate, it must be free of contaminants. Carbon and oxygen are the most familiar contaminants on the tungsten surface. In order to remove carbon impurities, the crystal has to be heated to 1200 °C, measured by a pyrometer, at an oxygen atmosphere (1×10^{-7}mbar). This step is used to remove the carbon from the surface through the reaction with oxygen admitted into the UHV system. The next step is electron bombardment heating at $T = 2000$ °C and to remove the oxide layer.

In situ scanning tunneling measurements have been carried out on mass filtered Fe_xNi_{1-x} nanoparticles. The microscope used is a MicroSPM from Omicron. The height of the nanoparticles after deposition and after melting at elevated temperatures was determined by STM. This heating cycle was carried at in such a way that the first step was heating for 30 min at 540 K followed by the investigation at room temperature. This system was taken for the second step consisting of heating for 30 min at 580 K with the following STM measurement at room temperature. Again, this system was taken for the third step with heating for 30 min at 840 K with investigation subsequently at room temperature. This means, all measurements were sebsequently conducted at room temperature, and the basic pressure was below 3×10^{-10} mbar. Additionally, the samples were prepared under identical conditions to study the melting of the nanoparticles when heated directly after deposition, maintaining a temperature of 840 K for 90 min (see Fig. 1). High resolution electron microscopy is required to shed light on the particle shape, and electron diffraction helps to identify the crystal structure and the distribution of elements inside the nanoparticles. Transmission electron microscopy (TEM), including high resolution imaging, was performed at 300 kV on the magnetic nanoparticles spread on the carbon-coated copper grid.

3. Result and discussion

Fe_xNi_{1-x} nanoparticles with sizes ranging from 3 to 6 nm were deposited on W(110) at room temperature and subsequently heated. Three types of FeNi alloys were used: $Fe_{0.75}Ni_{0.25}$, $Fe_{0.50}Ni_{0.50}$, $Fe_{0.25}Ni_{0.75}$. Additionally pure nickel and pure iron nanoparticles were investigated for comparison. Here, the properties of these nanoparticles after depositing on a W(110) and how they respond to heating are discussed.

3.1. Tempering

The STM images and height distribution of FeNi with three different compositions and Ni and Fe nanoparticles on the tungsten surface are shown in Fig. 2 after deposition at room temperature. All the particles were spherical in shape. In all cases, the nanoparticles were found to have no preferred adsorption sites. Instead, they accumulate randomly on both flat terraces, and on step edges.

In the first heating cycle, the nanoparticles were heated to 540 K for 30 min. Fig. 3 shows the particles after heating. The first change is the height of the nanoparticles: the nanoparticles exhibit a uniform height of approximately 2.5 Å, suggesting the formation of islands primarily consisting of one monolayer.

In the case of pure Fe nanoparticles, the diffusing Fe atoms have agglomerated at the step edges of the substrate. This indicates the high mobility of Fe atoms at 540 K. The merging of two islands can be observed, which probably proceeds according to the principle of dynamic coalescence. It can occur as a result of the collision of two islands, where mobile island diffuse across a surface to form a larger island when they collide [13]. The second possibility is the melting of two nanoparticles being nearby at the substrate after deposition.

Just like the Fe islands, the $Fe_{0.75}Ni_{0.25}$ islands exhibit a similar behavior by agglomerating at the step edges of the substrate within narrow terraces. These islands maintain their compact shape after undergoing a melting process. This observation highlights the similarity in the behavior between Fe islands and $Fe_{0.75}Ni_{0.25}$ islands.

Islands with a monoatomic height can be observed around some $Fe_{0.50}Ni_{0.50}$ nanoparticles due to the unrolling carpet behavior. For both Fe and Ni, this implies that a film of a single monolayer thickness, defined by a distinct boundary, extends across the surface. The assumption is made that the atoms within the initial layer remain stationary. On top of this initial layer, atoms undergo diffusion, once they reach the edge of the diffusion area and make contact with the substrate, where they become stuck.

The $Fe_{0.25}Ni_{0.75}$ particles are completely melted and they have a ramified shape. It is important to note that the temperature and duration of the tempering process are responsible for the formation of ramified islands after tempering. Compared to iron atoms at the same temperature, nickel atoms exhibit a lower mobility or have a stronger binding energy with the surface. In other words, Ni atoms are less likely to move or diffuse across the surface and are more strongly attracted to the surface compared to iron atoms.

The next higher temperature step was carried out for further 30 min at a temperature of approximately 580 K (Fig. 4). All samples showed islands of one monolayer in height.

There is no change in the shape of the iron islands after melting of pure Fe nanoparticles. They are all agglomerated at the step edges in narrow terraces.

Some islands of $Fe_{0.75}Ni_{0.25}$ show anisotropic spreading along the W[111] axes, caused by the crystallographic structure of the substrate. A noticeable feature is an island with a bulge on the side, which probably represents the merging of a larger island with a smaller one (coalescence). If this were to occur as a result of the collision of the two islands, this process would probably follow the principle of Smoluchowski ripening (dynamic coalescence).

The so-called Ostwald ripening might not be the underlying process in this particular case, since it involves a flow of material from a smaller to a larger island occurs, which is triggered by the system's drive for energy minimization [13]. In contrast, the bulge seen in Fig. 4 can presumably only occur when two islands collide, and consequently during Smoluchowski rifting. To check for the presence of Ostwald ripening, we investigate whether the frequency of small islands decreases in subsequent experiment stages. Smoluchowski ripening likely contributes to the development of larger islands. However, clear indications supporting this, based on all the provided images, are exceptionally rare. Thus, Smoluchowski ripening alone cannot be solely responsible for the

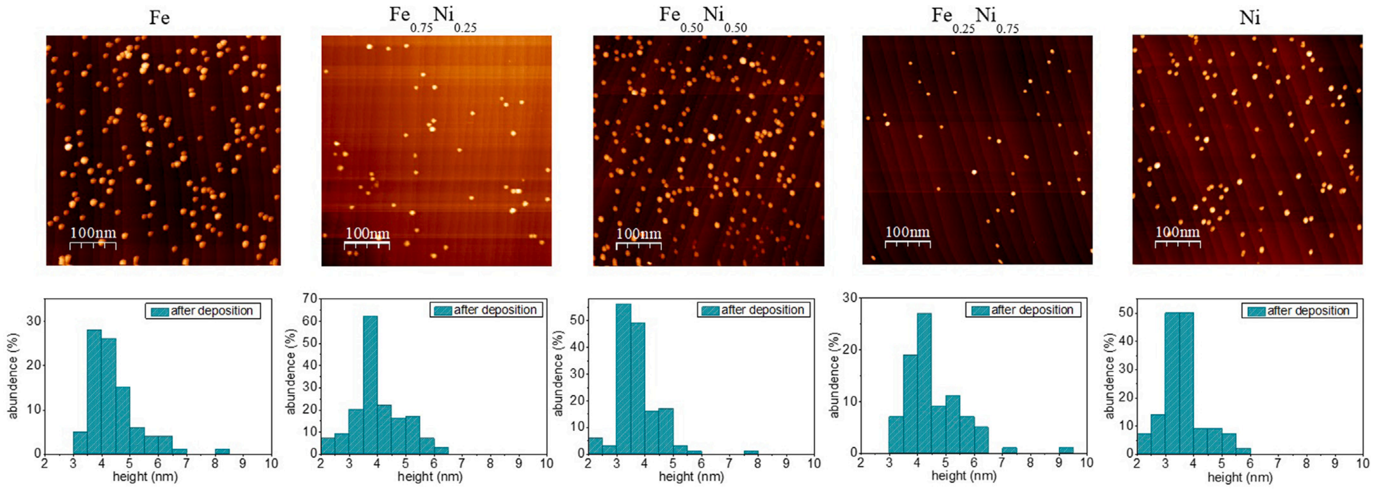

Fig. 2. STM images and the height distribution of the nanoparticles after the deposition process at room temperature.

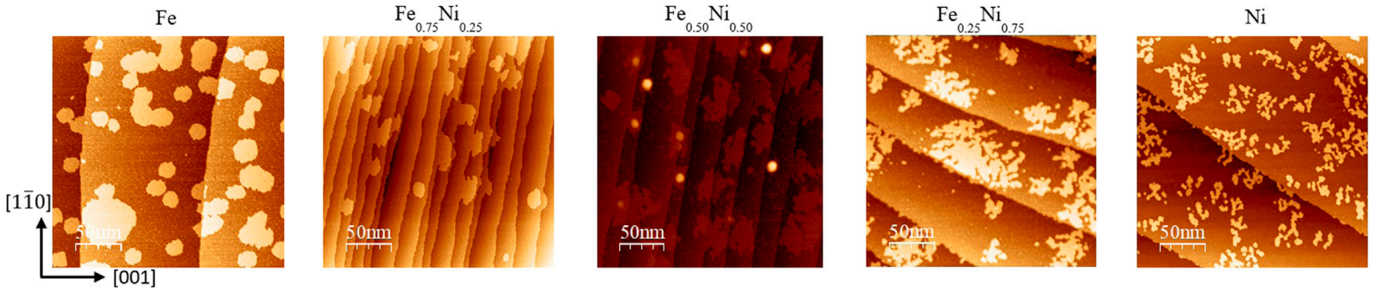

Fig. 3. STM image of Fe_xNi_{1-x} islands on W(110) after 30 min annealing at 540 K.

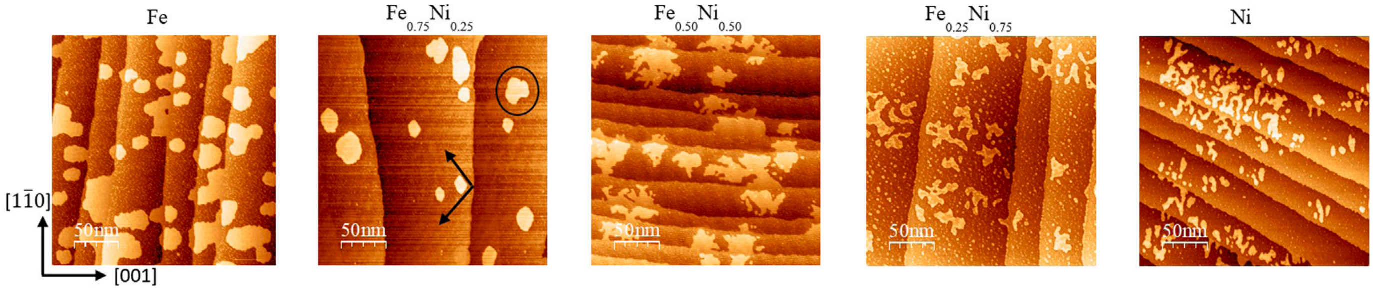

Fig. 4. STM image of Fe_xNi_{1-x} islands on W(110) after 30 min subsequently annealing at 580 K.

growth of the islands. Instead, it appears that Ostwald ripening is the primary driving force behind most of the island growth. This conclusion is drawn from the consistent presence of smaller-than-average islands in nearly all images, with their sizes remaining unchanged from the start to the end of the experimental stages. Since islands generally increase in size over the heating cycles, the consistent presence of small islands can only be attributed to Ostwald ripening and the subsequent evaporation of material.

The islands present in the remaining samples exhibit a distinctive branched configuration. This illustrates an important observation, the thermal conditions at 580 K were apparently insufficient to facilitate the transformation of the islands into a more tightly integrated structure. An interesting observation arises from the analysis of the images. There is a discernible pattern where wider terraces tend to host a greater number of islands compared to narrower terraces.

All islands have compact shape by further tempering at 840 K for 30 min. Fig. 5 shows that the Fe islands are even larger than before. A comparison of the STM images of Fe and Ni islands shows that the iron is able to form larger islands than nickel. This can be interpreted as a consequence of the higher mobility of iron compared to nickel.

Some small $Fe_{0.75}Ni_{0.25}$ islands have a hexagonal shape, with the edges and angles being of different lengths and sizes (see the marked islands). A possible explanation could be that in large islands the stress on atoms located at the edges of the island is not as great as in smaller islands. Therefore, the effort to leave this shape is not as strong as in smaller islands. In addition, the restructuring of larger islands involves a correspondingly larger number of atoms, so the process necessarily takes longer. It is also noticeable that wider terraces tend to host a greater number of larger islands compared to their narrower counterparts. Additionally, a notable observation is that the material is found exclusively on the terraces and is no longer present at the step edges. Finally, stretching in the [1$\bar{1}$0] direction can be caused by anisotropic diffusion of atoms on the tungsten surface. The surface of the W(110) crystal itself is anisotropic.

Since the stretching of the islands in the [1$\bar{1}$0] direction also occurs when the step edges are not aligned with this direction, it can be concluded that the observed stretching is solely influenced by the geometry

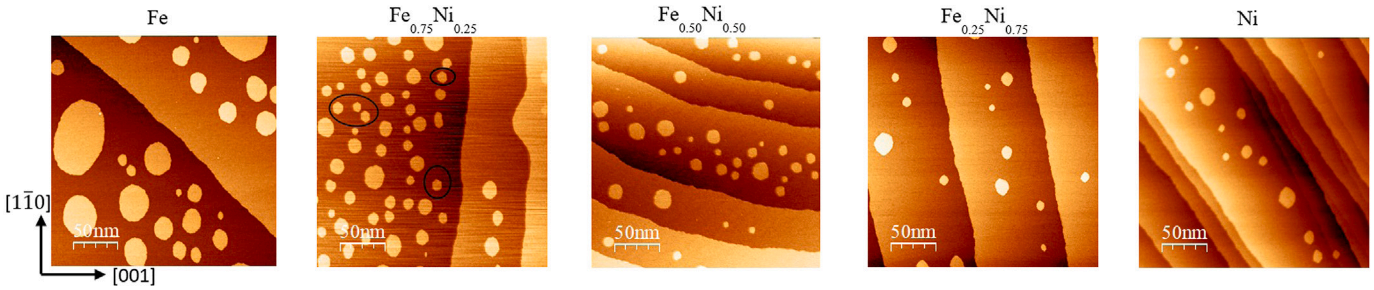

Fig. 5. STM image of Fe_xNi_{1-x} islands on W(110) after 30 min subsequently annealing at 840 K.

of the W(110) surface. Furthermore, considering that the heating was carried out at temperatures around 840 K, this is in agreement with the findings of Reuter et al. on the diffusion of nickel [14]. Additionally, it should be noted that the iron-nickel alloy adapts the behavior exhibited by iron and nickel alone at this temperature.

Regarding the $Fe_{0.50}Ni_{0.50}$ islands, it should be noted that the islands have formed only in a very narrow, defined area on the terraces, which is slightly shifted towards the sloped side. This and the fact that no islands can be observed at all on the narrow terraces leads to the assumption that material melts at the step edges of the tungsten substrate if it is close enough to them and is therefore no longer visible in the STM images. On the other hand on narrow terraces, the distance to the step edges is necessarily smaller/too small, hence no material is located there. In addition, the melting of an island on a step edge can be directly observed, which confirms the previous assumption.

For $Fe_{0.75}Ni_{0.25}$ islands, it is worth noting that a hexagonal structure is emerging, as indicated by the distinct edges observed in some of these islands. This structural transformation is evident over a wide range of island sizes. However, it is intriguing to observe that exceptionally large islands within this composition show no discernible signs of such structural reorganization. In contrast, $Fe_{0.25}Ni_{0.75}$ islands consistently adopt a hexagonal structure across all size variations. This observation suggests that the transition process in $Fe_{0.25}Ni_{0.75}$ islands appears to be independent of island size, highlighting the unique behavior of this composition.

Ni islands consistently take on a hexagonal form across various sizes, similar to $Fe_{0.25}Ni_{0.75}$. There are no islands present on the narrow terraces, and the step edges are rough. From this observation it can be concluded that the islands that were once on these terraces have undergone melting at these step edges.

3.2. Annealing at 840 k for 90 min directly after deposition

In order to evaluate whether there are differences in the final shape of the islands after sequential heating or immediate heating after deposition, samples were prepared under identical conditions. These samples were subjected to direct heating at 840 K for 90 minutes after deposition at room temperature. As can be seen in Fig. 6, hexagonal islands are no longer present. As predicted by Reuter et al. [14], the spreading behavior of Fe proved to be anisotropic, characterized by rapid expansion along the [110] direction and more gradual expansion along the [100] direction at 970 K. Remarkably, the configuration of the diffusion zone for Fe remained invariant, unaffected by both the initial material placement on the substrate and the annealing temperature up to 1070 K. As expected, the Fe nanoparticles melt completely and form a monolayer of uniform height after heating for 90 min immediately after deposition. These Fe islands have a compact and elliptical shape with the long axis along the $[1\bar{1}0]$. In contrast to Fe, the Ni islands begin to develop edges oriented in the [111] direction.

All $Fe_{0.75}Ni_{0.25}$ islands have an anisotropic stretching in the $[1\bar{1}0]$ direction, as shown in Fig. 7, which is caused by the crystallographic structure of the W(110) surface. Based on deductions drawn from experimental data obtained during growth experiments [15], it becomes evident that, in the cases of Fe and Ni, the initial monolayer undergoes pseudomorphic growth on the W(110) substrate, so they have bcc(110) structure. The inherent twofold symmetry of the bcc(110) surface naturally leads to anisotropic spreading, which accounts for the shape observed for FeNi islands.

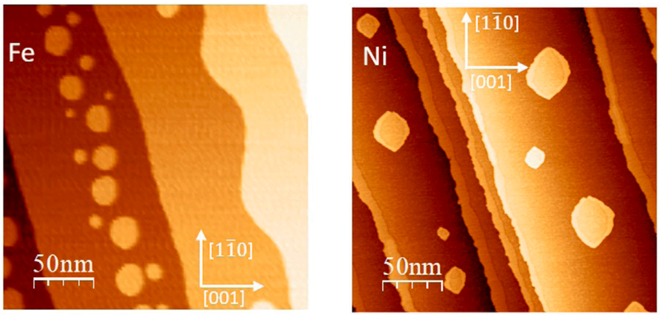

Fig. 6. STM image of Fe and Ni islands on W(110) after 90 min heating of the respective pure element nanoparticles at 840 K, directly after deposition.

As observed in Fig. 7, similar to our previous observations, the height of the islands corresponds to one monolayer. There is no noticeable change in the case of $Fe_{0.5}Ni_{0.5}$ with respect to the subsequently 30 min heat treatment at 840 K.

The melting of a $Fe_{0.25}Ni_{0.75}$ island at a step edge can be directly observed in Fig. 7. The islands have exclusively formed in a region slightly shifted to the sloped side, confirming the previous assumption. However, $Fe_{0.25}Ni_{0.75}$ have formed elongated islands.

3.3. Composition and structure

The melting temperature of FeNi nanoparticles depends on both their size and their specific structural configuration. In order to elucidate and improve our understanding of the melting behavior of these particles with different stoichiometric compositions, we performed a crystal structure analysis and elemental mapping of the nanoparticles. The aim of this approach was to gain insight into the underlying factors that influence the way in which these nanoparticles undergo the melting process. $Fe_{0.75}Ni_{0.25}$, $Fe_{0.50}Ni_{0.50}$, $Fe_{0.25}Ni_{0.75}$ nanoparticles were produced using the magnetron sputtering source and deposited on graphene oxides on Lacy carbon on Cu grids (Plano, 400 mesh). The data presented in Fig. 8 images were captured for a $Fe_{0.50}Ni_{0.50}$ nanoparticle using an image-corrected FEI Titan 80–300 transmission electron microscope. Additionally, HRSTEM analyses, including EDS data were acquired using a probe-corrected FEI Titan 80–300 transmission electron microscope. The microscope operates at a voltage of 300 keV and achieves a point resolution of 0.08 nm in TEM mode. The sample was exposed to the air during transfer to the microscope. This can lead to the formation of an oxide shell around the particles.

Notably, lattice fringes are observed, indicating the presence of a crystalline structure. Furthermore, by applying the Fast Fourier Transform (FFT) analysis to the images, distinct reflections are identified,

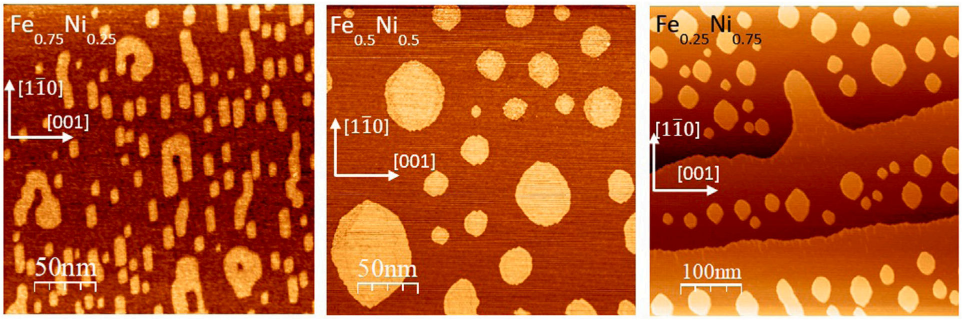

Fig. 7. STM image of Fe_xNi_{1-x} islands on W(110) after 90 min annealing at 840 K directly after deposition.

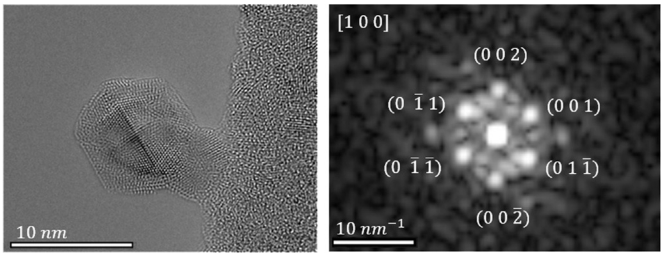

Fig. 8. (a) High resolution TEM image, (b) the corresponding FFT image of a $Fe_{0.50}Ni_{0.50}$ nanoparticle.

and their alignment with the [100] zone axis is confirmed. The FFT analysis helps in extracting and analyzing the spatial frequency information from the images. The presence of these prominent reflections at specific orientations indicates the crystallographic alignment of the nanoparticles.

In the case of bimetallic nanoparticles, it is important to assure that the elemental composition is the same as the stoichiometry of the target material. To obtain spatially resolved chemical information about the complex structure, both the full energy loss spectrum and energy dispersive X-ray analysis were utilized across a series of points on the nanoparticles. This approach allows for the extraction of linear compositional variations. In this work, due to the challenging signal-to-noise ratio and variations in nanoparticle orientation, this measurement cannot provide the correct stoichiometry, and quantification of the results was not possible. But it should be noted that with another type of source the stoichiometry of thr target is nearly identical with that of the alloy nanoparticles [16].

Fig. 9 visually displays the elemental mapping and the line profile across the particles. This line profile illustrates the intensity of Fe and Ni in both the vertical and horizontal directions. Two different directions were chosen to examine whether there are any variations in the elemental composition along the line scan.

For $Fe_{0.75}Ni_{0.25}$ (left column in Fig. 9), the line profile of Ni shows a distinct peak at the location of the particle core, while the spectra on either side of the core are dominated by Fe. At the core, the intensities of Fe and Ni are roughly equal. However, at the shell, there is a higher concentration of Fe, suggesting that Fe atoms are more likely to be found in these regions. On the other hand, the intensity of Ni at the edges is nearly zero. This increased Fe percentage at the edges can be explained by the nanoparticles having a higher atomic percentage of Fe compared to Ni, indicating a preferential distribution of Fe atoms towards the edges of the nanoparticle.

The EDS line profile of $Fe_{0.50}Ni_{0.50}$ demonstrates an equivalent intensity of Fe and Ni across the entire particle in both directions (middle column in Fig. 9). This finding suggests that nanoparticles with an equal composition of Fe and Ni have a uniform structure. The distribution of Fe and Ni elements within the particles is evenly dispersed, which is corroborated by the elemental mapping of the particle. This means that there is no significant variation in the concentration or arrangement of Fe and Ni atoms across the particle.

The EELS line scan profile of $Fe_{0.75}Ni_{0.25}$ in the right column Fig. 9 reveals a notable peak in the Ni intensity at the particle's core position, indicating a predominant presence of Ni atoms in the core region. Conversely, the Fe intensity is distributed uniformly across the entire particle, suggesting a more even distribution of Fe atoms.

To better understand the results, a mathematical approach using error functions was utilized. This method helps us to depict how materials are distributed within a core–shell structure. Imagine a round particle: as you go from the center towards the surface, we are interested in how the concentration of different materials changes. The radius of the core is denoted as r_1 and the radius of the shell is denoted as r_2 (see Fig. 10). So, the line distribution of the material in the core is expressed as:

$$s_1 = 2\sqrt{2r_1(x-d)-(x-d)^2}$$

likeweis the Line distribution of material in the shell is expressed as:

$$s_2 - s_1 = 2\sqrt{2r_2x - x^2} - 2\sqrt{2r_1(x-d)-(x-d)^2}$$

where d represents the thickness of the shell.

In theory, the set of these two functions has the potential to characterize any STEM-EDX map derived from a spherical core/shell particle with a distinct interface and surface. In the specific systems that were investigated in this research, a notable portion of the material from the core is found within the shells of the particles. Additionally, the material constituting the shell is dispersed throughout the structure. This complex arrangement contrasts with the ideal scenario of a clear distinction between the core and shell. To tackle this complex configuration and the lack of a well-defined core–shell boundary, certain modifications are made to the equations, so that the radial distribution of Fe and Ni is expressed as:

$$c_{Ni} = s_1 + p(s_2 - s_1)$$

$$c_{Fe} = s_2 - qs_1$$

where p and q represent the proportion of the remaining core material in the shell. We also used error functions to estimate the boundary between the core and the shell. The distribution pattern of the elements as revealed by this analysis is depicted in Fig. 11. The measurement identified a broadening of 0.3 nm at the core/shell interface. The core primarily contains Ni atoms, and the fraction of Ni is higher in the core compared to Fe. This means that Ni atoms prefer to be concentrated in the core region. As we move from the core to the shell, the fraction of Ni atoms gradually decreases, creating a decreasing gradient of Ni concentration. However, even in the shell, some Ni atoms are still present, but their fraction is lower compared to the core. In contrast, the arrangement of Fe atoms is different. Fe atoms have a greater tendency to disperse throughout the particle. However, the proportion of Fe atoms within the shell is significantly greater than that within the core. It is worth noting that a noticeable fraction of Fe remains in

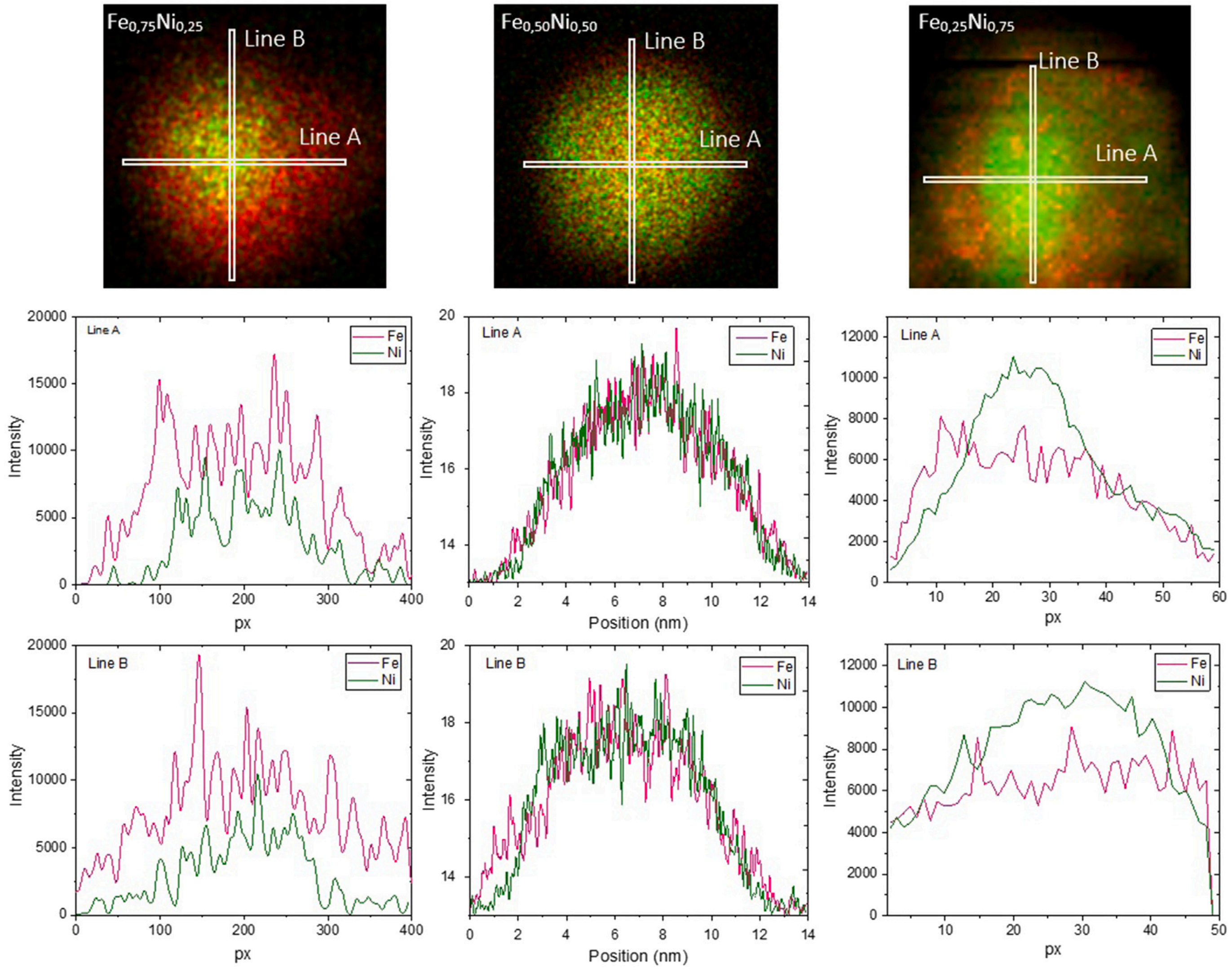

Fig. 9. High resolution STEM image of an Fe_xNi_{1-x} nanoparticle with different stoichiometry (top row), where the colored representation depicts the qualitative overlay of Fe and Ni concentrations. Accompanying by line scan profile of the nanoparticles (bottom rows) in two directions.

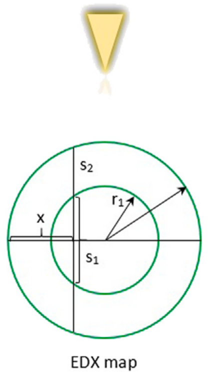

Fig. 10. Schematic representation of the acquisition of a STEM-EDX map of a core–shell nanoparticle.

the core, and its contribution is particularly pronounced in the case of $Fe_{0.75}Ni_{0.25}$ particles. This observation (Fig. 11) suggests a preferential distribution of Ni towards the core region, indicating that Ni atoms have a higher affinity for occupying the central positions within the particle structure. On the other hand, Fe atoms tend to reside closer to the outer regions, resulting in their prevalence at the particle's surface. So, the core of the nanoparticle is enriched with Ni atoms, while the shell has a higher fraction of Fe atoms. The transition from the core to the shell leads to a gradual decrease in Ni concentration and a relative increase in Fe concentration.

As can be seen in this work, variations occur in bimetallic systems with the same size range but different compositions upon heating. In the case of $Fe_{0.75}Ni_{0.25}$ and $Fe_{0.25}Ni_{0.75}$, where a Ni core is surrounded by an Fe shell, all nanoparticles completely liquefy upon the first heating cycle (540 K). $Fe_{0.75}Ni_{0.25}$ islands consolidate into compact formations, while $Fe_{0.25}Ni_{0.75}$ adopt more branched structures. This difference is attributed to the robust bonding between Ni and the surface. In contrast, the $Fe_{0.50}Ni_{0.50}$ nanoparticles, characterized by an alloy structure, where Fe and Ni are homogeneously dispersed within the particle only initiate melting around 540 K. During this process, they exhibit an unrolling carpet behavior. This phenomenon indicates that the FeNi nanoparticles with an alloy structure possess a higher melting temperature than those with a core–shell configuration. This holds true when compared to particles with either a higher or lower Ni content.

In addition, the nanoparticles begin to melt from their outermost shell. In the case of $Fe_{0.75}Ni_{0.25}$ nanoparticles, it is important to note that the outermost layer is predominantly Fe. This structural feature is responsible for the remarkable similarity between the way

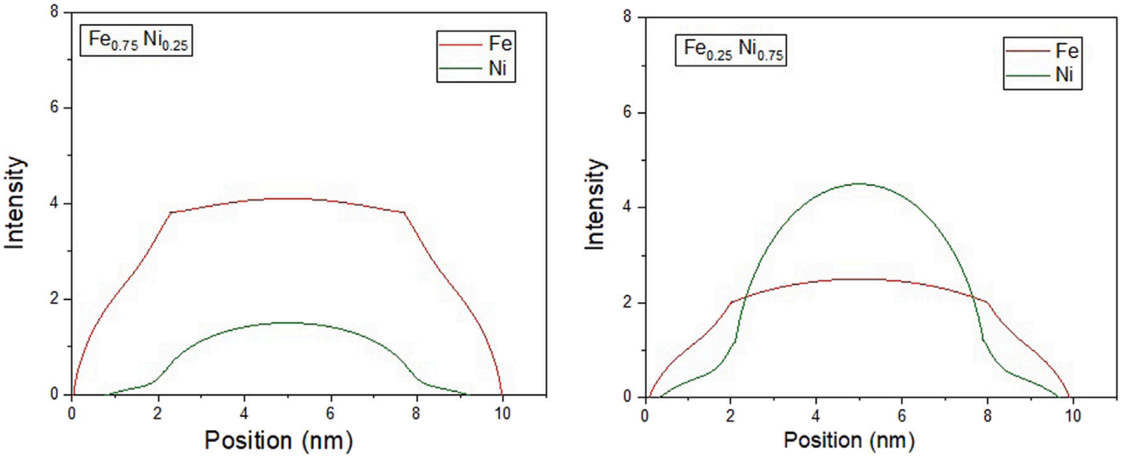

Fig. 11. Radially averaged EDX data with corresponding stoichiometry include a δ-function for a nonsharp interface.

these nanoparticles melt on tungsten and the behavior of pure Fe nanoparticles during melting processes.

4. Conclusions

In conclusion, the study of FeNi nanoparticles with three different compositions as well as pure Ni and Fe nanoparticles on a tungsten surface has provided valuable insights into their structural evolution and behavior during heating cycles. Significant changes were observed upon the first heating cycle. The nanoparticles underwent a transformation, forming compact islands with a height of a monolayer thickness. The agglomeration of diffusing Fe atoms at the step edges indicated high mobility at this temperature. Subsequent heating to approximately 580 K maintained the one-monolayer height of the islands, with the FeNi islands showing anisotropic spreading along the W[111] axes. However, the thermal conditions at this temperature were insufficient to induce a more compact structure, leading to the persistence of distinctive branched configurations. Further heating at 840 K resulted in all islands adopting a compact shape, with Fe islands growing larger than Ni islands. The temperature-induced restructuring demonstrated the impact of the higher mobility of iron compared to nickel. Interestingly, the presence of material exclusively on terraces and not on step edges, coupled with the observation of wider terraces hosting more islands, suggests a correlation between terrace width and island distribution.

The analysis of the distribution pattern of elements within the FeNi nanoparticles indicates a preference for Ni concentration in the core and Fe dispersion in the shell of FeNi nanoparticles. In addition, variations in melting behavior highlight the influence of composition, with alloy structures exhibiting higher melting temperatures compared to core–shell configurations.

CRediT authorship contribution statement

Mahboobeh Ravankhah: Investigation, Writing – original draft. **Philipp Watermeyer:** Investigation, Visualization, Writing – original draft. **Gerhard Dehm:** Funding acquisition, Project administration, Resources, Supervision, Writing – review & editing. **Mathias Getzlaff:** Conceptualization, Funding acquisition, Investigation, Project administration, Resources, Supervision, Validation.

Declaration of competing interest

The authors declare that they have no known competing financial interests or personal relationships that could have appeared to influence the work reported in this paper.

Data availability

No data was used for the research described in the article.

References

[1] X. Liu, X. Liu, Bimetallic nanoparticles: kinetic control matters, Ang. Chem. Int. Ed. 51 (14) (2012) 3311–3313.
[2] J. Teeriniemi, M. Melander, S. Lipasti, R. Hatz, K. Laasonen, Fe–Ni nanoparticles: A multiscale first-principles study to predict geometry, structure, and catalytic activity, J. Phys. Chem. C 121 (3) (2017) 1667–1674.
[3] Z. Yang, Q. Wang, X. Shan, W.-q. Li, G.-h. Chen, H. Zhu, DFT study of fe-Ni core-shell nanoparticles: Stability, catalytic activity, and interaction with carbon atom for single-walled carbon nanotube growth, J. Chem. Phys. 142 (7) (2015).
[4] Y.J. Suh, H.D. Jang, H. Chang, W.B. Kim, H.C. Kim, Size-controlled synthesis of Fe–Ni alloy nanoparticles by hydrogen reduction of metal chlorides, Powder Technol. 161 (3) (2006) 196–201.
[5] Y. Liu, Y. Chi, S. Shan, J. Yin, J. Luo, C.-J. Zhong, Characterization of magnetic NiFe nanoparticles with controlled bimetallic composition, J. Alloys Compd. 587 (2014) 260–266.
[6] B. Shao, Y. He, J. Lai, D. Chen, D. Guo, Y. Ma, Preparation of Ni 1- x Fe x nanoparticles with a composition gradient and a proposed formation mechanism, J. Nanoparticle Res. 22 (2020) 1–11.
[7] O. Margeat, D. Ciuculescu, P. Lecante, M. Respaud, C. Amiens, B. Chaudret, NiFe nanoparticles: a soft magnetic material? Small 3 (3) (2007) 451–458.
[8] E. Parks, K. Kerns, S. Riley, The structure of nickel–iron clusters probed by adsorption of molecular nitrogen, Chem. Phys. 262 (1) (2000) 151–167.
[9] H. Bettermann, M. Werner, M. Getzlaff, Temperature-induced processes for size-selected metallic nanoparticles on surfaces, Appl. Surf. Sci. 391 (2017) 49–52.
[10] W. Rosellen, C. Kleinhans, V. Hückelkamp, F. Bulut, A. Kleibert, J. Bansmann, M. Getzlaff, Influence of substrate and temperature on the shape of deposited fe, co, and FeCo nanoparticles, Phys. Status Solidi (B) 247 (5) (2010) 1032–1038.
[11] W. Rosellen, H. Bettermann, T. Veltum, M. Getzlaff, Low energy impact of size selected FeCo nanoparticles with a w (1 1 0) surface, Physica E 44 (7–8) (2012) 1683–1686.
[12] Oxford Applied Research, NC200U Nanocluster Source Application Note, Oxford Applied Research.
[13] K. Oura, V. Lifshits, A. Saranin, A. Zotov, M. Katayama, Surface science: an introduction, Springer Science & Business Media, 2013.
[14] D. Reuter, G. Gerth, J. Kirschner, Anisotropic diffusion of 3 d metals on w (110): Competition between crystalline structure and surface steps, Phys. Rev. B 57 (4) (1998) 2520.
[15] H. Elmers, J. Hauschild, H. Höche, U. Gradmann, H. Bethge, D. Heuer, U. Köhler, Submonolayer magnetism of fe (110) on W (110): Finite width scaling of stripes and percolation between Islands, Phys. Rev. Lett. 73 (6) (1994) 898.
[16] M. Getzlaff, J. Bansmann, F. Bulut, R. Gebhardt, A. Kleibert, K. Meiwes-Broer, Structure, composition and magnetic properties of size-selected feco alloy clusters on surfaces, Appl. Phys. A 82 (2006) 95–101.